1  **Time resolution in cryo-EM using a novel PDMS-based microfluidic chip**

2  **assembly and its application to the study of HflX-mediated ribosome**

3  **recycling**

4

5  Sayan Bhattacharjee[1,#], Xiangsong Feng[1,#*], Suvrajit Maji[1], Prikshat Dadhwal[2],

6  Zhening Zhang[1], Zuben P. Brown[1,3], Joachim Frank[1,2*†].

7

8  [1]Department of Biochemistry and Molecular Biophysics, Columbia University, New

9  York, NY 10027, USA

10  [2]Department of Biological Sciences, Columbia University, New York, NY 10027,

11  USA

12  [3]Current address: Thermo Fisher Scientific, Oregon, USA

13  [#]These authors contributed equally

14  [*] Corresponding Authors

15  [†]Lead Contact

16

17  The rapid kinetics of biological processes and associated short-lived

18  conformational changes pose a significant challenge in attempts to structurally

19  visualize biomolecules during a reaction in real time. Conventionally, on-

20  pathway intermediates have been trapped using chemical modifications or

21  reduced temperature, giving limited insights. Here we introduce a novel time-

22  resolved cryo-EM method using a reusable PDMS-based microfluidic chip

23  assembly with high reactant mixing efficiency. Coating of PDMS walls with

24  $SiO_2$ virtually eliminates non-specific sample adsorption and ensures

25  maintenance of the stoichiometry of the reaction, rendering it highly

26  reproducible. In an operating range from 10 to 1000 ms, the device allows us

27  to follow in vitro reactions of biological molecules at resolution levels in the

28  range of 3 Å. By employing this method, we show for the first time the

29  mechanism of progressive HlfX-mediated splitting of the 70S *E. coli* ribosome

30  in the presence of the GTP, via capture of three high-resolution reaction

31  intermediates within 140 ms.

32

33  **Introduction**

34

35  To comprehend the fundamentals of any biological process, one requires

36  insights into the underlying molecular mechanisms. It is often possible to study

37  a reaction in vitro, outside the context of the cell. However, interactions among

38  reactants and concurrent conformational changes of the molecules are too fast

39  to be captured structurally using standard methods of biophysical imaging. In

40  single-particle cryo-EM, the conventional pipetting-blotting method of sample

41  deposition on the grid requires several seconds at least -- too long to capture

42  reaction intermediates of molecular machines, which are in the range of tens

43  or hundreds of milliseconds. In the past, some of such intermediates have been

44  trapped by the use of non-hydrolysable analogs (such as GMP-PNP[1,2],

45  antibiotics[3], or cross-linking[4]), but the insights gained in this way are limited

46  and often burdened with presumptions.

47      Time-resolved cryo-EM (TRCEM) opens a way for obtaining structural

48  and kinetic information on reaction systems that are not in equilibrium but

49  change over time until equilibrium is reached[5]. In TRCEM studies, the

50  biological reaction is started by mixing reactants, then stopped at a selected

51  time point by fast-freezing, and the so trapped reaction intermediates are

visualized by single-particle cryo-EM. By means of multiple experiments with different time points, TRCEM is able to capture the time course of a reaction, leading to a 'movie' of intermediates on the path to the state in equilibrium[6].

Over the years, a variety of TRCEM methods have been developed[7-19] showing the potential for obtaining key insights into the mechanism of action of molecules and molecular machines on the time scale of tens to hundreds of milliseconds. These methods can be divided into two categories: spraying/mixing[15] and mixing/spraying[10]. In the first category, a specialized sprayer[15] or dispenser system[7] is employed to deposit one reactant onto a grid already covered with another reactant. Both mixing and reacting occur on the grid immediately prior to vitrification. Questions have been raised over the uniformity of a diffusion-dependent reaction on the grid[6]. In addition, electron tomography has shown that molecules are frequently observed to congregate at the top and bottom of the ice layer[20], raising concerns about artifacts stemming from their extended exposure to the air-water interface in spraying/mixing or dispensing/mixing methods. In the second category, a microfluidic chip is used for mixing and reacting two reactants and for subsequent rapid spraying to deposit the reaction product onto the grid, followed immediately by plunging of the grid into the cryogen[8-10,12-14,16]. In that case, mixing and reacting can be efficiently controlled, and the time during which the reaction product is exposed to the air-water interface is kept minimal.

There are still some key issues among the existing methods which need to be resolved. One problem is sample adsorption on the walls of the chip. Polymers such as PDMS, IP-S, IP-Q are now commonly used as a cost-

77  effective material to fabricate microfluidic chips[12,13,18,19], but as a rule, the

78  surfaces of these materials are intrinsically hydrophobic and adsorb a

79  substantial amount of protein. In this case, the contact between the sample and

80  the polymer microchannel can degrade the quality of the reaction, casting

81  doubt over the accuracy of the kinetic information. This problem is avoided

82  with silicon-based microfluidic chips[16,17] which are by nature hydrophilic, but

83  they are quite impractical as it takes several weeks and on average hundreds of

84  dollars to manufacture a chip of a specific design (i.e., in multiple copies; with

85  production steps including the etching and dicing of a silicon wafer and

86  bonding it with glass). Another problem is insufficient initiation of a reaction,

87  which may result from ineffective mixing of fluids due to limited micromixer

88  performance[12,14] in the laminar flow regime.

89       In the following we describe our TRCEM setup utilizing a PDMS-based

90  microfluidics chip assembly of new design that overcomes these problems, as

91  it efficiently mixes the reactants for uniform initiation of a reaction, conducts

92  a controlled reaction virtually unimpeded by protein adsorption, and sprays the

93  reaction product in a uniform three-dimensional cone onto the EM grid. We

94  have used this novel device successfully in several studies on translation. Here

95  we present the study of HflX-mediated recycling in detail to demonstrate the

96  efficacy of the novel TR device, and its capability to yield biologically

97  significant information.

98       **H**igh **f**requency of **l**ysogenization **X** (HflX) is a universally conserved

99  protein for prokaryotes, a GTPase which acts as a ribosome-splitting factor in

100  response to heat shock or antibiotics[2,21-23]. *E. coli* HflX consists of four

101  domains: N-terminal domain (NTD), GTP binding domain (GBD), C-terminal

4

102   domain (CTD), and helical linker domain (HLD)[2,24]. The cryo-EM structure of

103   the HflX-50S complex stalled in the presence of GMP-PNP, a non-

104   hydrolysable GTP analog, revealed that the HLD and NTD of HflX bind to the

105   peptidyl-transferase center, presumably causing rupture of the intersubunit

106   bridge B2a (h44:H69), thereby promoting the dissociation of the 70S

107   ribosome[2]. However, the molecular mechanism of these events and particularly

108   the interaction between HflX and 70S have remained elusive. Using TRCEM,

109   we were able to capture three short-lived intermediate states, at resolutions in

110   the 3-Å range, by starting the reaction between HflX and the *E. coli* 70S

111   ribosome in the presence of GTP and stopping it at 10, 25 and 140 ms. Atomic

112   models of these states allowed us to elucidate the mechanism of this process in

113   great detail.

114

115   **Results**

116   **A novel microfluidic chip assembly for TRCEM**

117   The complete setup for TRCEM grid preparation, originally based on an

118   apparatus built by Howard White[25], is depicted in Figure S2. The heart of the

119   TR apparatus is the microfluidic chip assembly mounted next to the plunger

120   (Figure 1A), which are both accommodated in an environmental chamber that

121   maintains the temperature and humidity at controllable levels. The plunger,

122   which is pneumatically operated, holds the tweezers on which the EM grid is

123   mounted for fast plunging into liquid ethane after passing the spray cone. In

124   addition, the apparatus contains the pumping system for introducing the

125   solutions into the micro-mixer and the nitrogen gas into the gas inlets of the

126    micro-sprayer. Finally it also houses the computer for controlling both the

127    pumping system and the plunger.

128        We designed and successfully tested the modular TR chip assembly

129    shown in Figure 1B, which is composed of three elements/modules: 1) a $SiO_2$-

130    coated, PDMS-based splitting-and-recombination (SAR) micro-mixer with 3D

131    self-crossing channels (Figure 1C), which is able to mix the solutions with the

132    effectiveness of > 90% at working flowrate of 6 µL/s (Figures 1E and S3, and

133    Methods section in Supplemental Information(SI)); 2) a micro-capillary glass

134    tubing serving as the micro-reactor for stable (i.e., unchanged under conditions

135    of high pressure drop) reaction time control (Figure S4, and Methods section

136    in SI); 3) a PDMS-based micro-sprayer with inner capillary tubing for spraying

137    out the reaction product under the action of pressurized nitrogen gas (Figure

138    1F, Methods section in SI, and supplemental video 1).

139        To prevent adsorption of molecules, plasma-enhanced chemical vapor

140    deposition (PECVD) is used to coat the inside walls of the PDMS micro-mixer

141    channels with a thin $SiO_2$ layer. We tested the sample adsorption with the *E.*

142    *coli* 70S ribosome to compare the chips without coating to those with DDM or

143    $SiO_2$ coating. The sample concentration in buffer is measured before and after

144    passing the devices with different types of coatings by our Nanodrop UV-Vis

145    Spectrophotometer (see Methods section in SI). In this experiment, 94% of the

146    initial concentration was retained using the $SiO_2$-coated chip (Figure 1H and

147    Table S2), while only 54% and 60% were retained after the sample was passed

148    through the chip assembly without coating or with DDM coating, respectively.

149    These findings demonstrate that the $SiO_2$ coating can effectively mitigate the

150    sample adsorption for ribosomes. After one month, the $SiO_2$-coated chip

151   assembly was tested again with 70S ribosome and HflX protein, and 92% of

152   the 70S and 93% of HflX were shown to be still retained, respectively (Figure

153   1I). These results demonstrate that the hydrophilicity of the internal surface is

154   virtually undiminished after a substantial period of time.

155       Thus it is apparent that the solutions introduced from the glass-capillary

156   liquid inlets will pass through the entire microfluidic device ($SiO_2$-coated

157   micromixer, glass-capillary micro-reactor and glass-capillary inner tubing of

158   the micro-sprayer) without contact with any hydrophobic surface, a fact of high

159   importance for preserving the stoichiometry of a reaction and guaranteeing its

160   reproducibility.

161       Based on these initial test results, we fabricated a set of microfluidic

162   chips (Figure 1G) to conduct a set of biological experiments. The relevant

163   materials and parameters for the fabrication of the chip assemblies are listed in

164   Table S1. An estimation of reaction times achieved using this TRCEM method

165   in the application to HflX-mediated ribosome recycling is given in the Methods

166   section in SI. Four microfluidic chip assemblies were used, with reaction times

167   estimated to be 10, 25, 140, and 900 ms, respectively.

168

169   **Exposure-targeting strategy in data collection for droplets-based cryo-**

170   **grids**

171   For grids obtained by the conventional blotting method, data collection is

172   usually done automatically after the template is set up for targeting both the

173   holes and exposures. But for grids prepared by the mixing-spraying method, it

174   is not easy to use automation, since every collectible square possesses droplets

175    of different sizes and thicknesses[25]. Hence time-consuming manual exposure

176    targeting is required.

177         Some observations on typical particle distributions in the HflX

178    experiment, to be detailed below, and other experiments led us to develop an

179    effective strategy for exposure targeting in data collection on droplet-based

180    grids.

181         There are two types of situations: one is where the droplet has no contact

182    with the grid bar (marked red in Figure S8); and the other where it does have

183    contact with the grid bar (marked green in Figure S8). In the former, the ice is

184    observed to be thick and unsuitable for data collection, while in the latter, there

185    is always some part of the region near the grid bar with an ice thickness suitable

186    for data collection. All our exposure targets are therefore focused on the second

187    type of droplets, as detailed below.

188         In the beginning, as shown in Figure 2A, we tried to collect data on as

189    many holes as possible for droplets of the second category, i.e., touching or

190    partially covering the grid bar, and found that typically there are four regions

191    with different behaviors, following a trend: (i) very close to the grid bar, as in

192    the area marked blue, the ice is not vitrified very well but particles are still

193    visible; (ii) in the area marked cyan, particles are clearly visible; (iii) further

194    on, in the area marked yellow, the number of the particles has significantly

195    decreased; until, (iv) in the area marked red, there are almost no particles left

196    (Figure 2A). In the present instance of data collection, only 170 out of 580

197    micrographs, or 29%, were left for data processing.

198         In line with these observations, we developed the exposure-targeting

199    strategy shown in Figure 2B: we collect only along two or three lines of holes

200  which are near and parallel to the grid bar, in the areas of type (i), (ii) and (iii).

201  As a result, in our example, we obtained 3433 good micrographs out of a 4458

202  total, which means about 77% could be used in this case for data processing.

203  We therefore adopted this strategy for all our data collection on grids prepared

204  by TR cryo-EM.

205

206  **Time-resolved experiments on HflX-mediated ribosome recycling from 10**

207  **to 900 ms**

208  HflX acts on the 70S ribosome in a nucleotide-dependent way, and light

209  scattering analysis revealed that the rate of ribosome splitting by HflX-GTP

210  $(0.002 \text{ s}^{-1})$ is very similar to the rate of ribosome dissociation by the combined

211  action of RRF and EF-G-GTP $(0.005 \text{ s}^{-1})$[22,26]. The fraction of ribosomes split

212  into subunits at room temperature within a reaction time of 140 ms is close to

213  50%, according to our earlier TR cryo-EM experiment on *E. coli* ribosome

214  recycling in the presence of RRF, EF-G, and GTP[9]. In view of these findings,

215  we anchored our TR cryo-EM study at a 140 ms reaction time point and added

216  two shorter time points (10 ms and 25 ms) and one longer one (900 ms) toward

217  the reaction's completion. We mixed 70S ribosomes with the HflX-GTP

218  complex in our mixing-spraying TRCEM apparatus (Figure S2) using different

219  microfluidic chips of the PDMS-based design (Figure 1G and Methods section

220  in SI). As in our previous TRCEM studies[9,10], 3D classification was performed

221  on the entire, pooled dataset across all four time points. The 3D classification

222  produced seven distinct classes, which we characterized by examining the

223  corresponding reconstructed density maps (note: "rotated" and "nonrotated"

224  refers in the following to the presence or absence of intersubunit rotation[27]):

225   (1) rotated 70S without HflX (r70S$_{noHflX}$); (2) non-rotated 70S without HflX

226   (nr70S$_{noHflX}$); (3) 70S-like intermediate-I with HflX (i70S$_{HflX}$-I); (4) 70S like-

227   intermediate-II with HflX (i70S$_{HflX}$-II); (5) 70S-like intermediate-III with HflX

228   (i70S$_{HflX}$-III); (6) 50S with HflX (50S$_{HflX}$); and (7) 30S (Methods section in SI

229   and Figures S10, and S11).

230        The splitting reaction kinetics of the 70S ribosome, as evaluated by

231   counting the numbers of particles obtained upon 3D classifications from 10 ms

232   to 900 ms, is found to follow a similar, roughly exponential behavior as

233   reported from dissociation kinetics measured by light scattering[2] (Figure 3M).

234   Furthermore, we noticed a rapid increase in the number of free 30S subunit

235   particles from 140 ms to 900 ms, which leads us to conclude that the final

236   separation of the subunits commences not earlier than with state i70S$_{HflX}$-III

237   (Figure 3M).

238

239   **Intermediate states of HflX-mediated recycling and their interpretation**

240   The three classes of HflX-containing intermediates and class 50S$_{HflX}$ -- four of

241   the seven 3D classes we found -- were selected for additional structural

242   analysis (Methods section in SI and Figures S10, and S11A-E). Furthermore,

243   focused 3D classification and subsequent reconstruction of HflX-binding

244   regions from each of the resulting class reconstructions yielded high-resolution

245   density maps for four states of HflX: (1) HflX-I, (2) HflX-II, (3) HflX-III, and

246   (4) HflX-IV (Figure S10). Refinement on the three i70S$_{HflX}$ class

247   reconstructions yielded high-resolution on-pathway intermediates i70S$_{HflX}$-I,

248   i70S$_{HflX}$-II, and i70S$_{HflX}$-III (Figures 3A-H), and their resolutions are indicated

249   in Figure S12 and Table S3.  The kinetics of the reaction can be followed from

250  the histogram of particle counts in the respective classes (Figure 3M). The

251  intermediates i70S$_{HflX}$-I, i70S$_{HflX}$-II, and i70S$_{HflX}$-III are each dominant in the

252  10 ms, 25 ms, and 140 ms time points, respectively, but are always intermixed

253  with the other intermediates, as well as with apo-70S, and the 50S-HflX end

254  product.

255      In all three intermediates, the CTD of HflX is found anchored to uL11

256  of the 50S subunit at the bL12 stalk base. Overall the comparison of the

257  intermediates shows a gradual clamshell-like opening of the 70S ribosome (see

258  supplemental video 2).

259      Structurally, the intermediates are distinguished by (i) the degree of the

260  clamshell-like opening, (ii) the position of helix H69 (in two steps, from

261  i70S$_{HflX}$-I to -III), (iii) the position of helix H71 (from i70S$_{HflX}$-I to -II), and

262  (iv) the position of HflX with respect to the 50S subunit (from i70S$_{HflX}$-I to -II,

263  and reversed from -II to -III). In the final state observed, after the departure of

264  the 30S subunit, HflX remains bound to the 50S subunit.

265      Comparison of the atomic models obtained for these intermediates with

266  one another and with the apo-70S revealed that the opening and splitting of the

267  70S ribosome occurs in the following steps:

268      First, the ribosome opens slightly to accommodate the initial binding of

269  HflX in i70S$_{HflX}$-I (Figures 3A, 3E-F). Using the tool previously developed[28]

270  we find that in this first intermediate, the 30S subunit has rotated by 5.9°

271  around an axis (Axis I) that passes through the intersubunit bridges B1b, B2a,

272  B3, and B4  (Figures 6A, D, G, and 6J-K), and this rotation has moved protein

273  bS6 of 30S into close vicinity to protein uL2 of the 50S subunit (Figures 3I-J).

274  Apparently, the insertion of HflX along with the prying apart of the 70S

275  ribosome and the rotation of the 30S subunit is driven by the increase in

276  backbone entropy of uL2 in i70S$_{HflX}$-I compared to apo-70S since we find

277  indications of disorder: the density of uL2 is not resolved well in i70S$_{HflX}$-I

278  (Figure 3J) compared to all its other manifestations in apo-70S, i70S$_{HflX}$-II and

279  i70S$_{HflX}$-III (Figures 3I-J, and S13). Comparison of the 50S subunit in i70S$_{HflX}$-

280  I and apo-70S shows that H69 has moved by 6.7 Å, apparently through a push

281  by HflX since fitting the model of HflX to apo-70S reveals a steric clash with

282  H69 (Figure 3K-L). In i70S$_{HflX}$-I HflX is blurred, indicating motion-induced

283  heterogeneity of the population in that class (Figure S10).

284      Going from this first intermediate to i70S$_{HflX}$-II and i70S$_{HflX}$-III we

285  observe stepwise rotations, by 7.9° and 8.2°, respectively, of the 30S subunit

286  around a new axis (Axis II) passing through intersubunit bridges B3 and B7a,

287  which are both located along helix h44 (Figures 3B-C, 3F-H, and 6B-C, 6E-F,

288  6H-I, and 6J-K). In the first step of rotation around this new axis, protein bS6

289  moves away from protein uL2 (Figures 3B, 3F-G, and 6B, 6E, 6H, and 6J-K).

290  This movement is made possible by a 6.5-Å pull of C1965 of H71 as a result

291  of HflX moving from its previous position on i70S$_{HflX}$-I to a new position on

292  i70S$_{HflX}$-II and a subsequent shift of the loop-helix motif (G74-V100)

293  associated with the NTD of HflX (Figures 4D-G). As a consequence, bridge

294  B3 (h44:H71), as well as bridges B7b and B7bR, have become destabilized.

295  While the conformation of the 30S subunit remains virtually the same from

296  apo-70S to the first intermediate, the change from the first to second

297  intermediate is accompanied by a rotation of the 30S subunit head by 2.1°

298  around another axis, Axis III (Figure S14).

299    In the second step of the 30S subunit rotation around Axis II, from

300    i70S$_{HflX}$-II to i70S$_{HflX}$-III, protein bS6 has continued to move away from

301    protein uL2 (Figure 3C, 3F-H, and 6C, 6F, 6I, and 6J-K), and HflX has shifted

302    back to its original position on the 70S ribosome in i70S$_{HflX}$-I. Bridges B7b and

303    B7bR are now entirely disrupted, allowing the flexible loop (E323-G349) of

304    HflX's GTD to readily access the 30S subunit protein uS12, thus positioned to

305    jettison the 30S subunit from the 70S ribosome (Figure 4A-C).

306    Finally, the reconstruction of the stable 50S-HflX complex, at 3.6-Å

307    resolution (Figures 3D, and S15A), no longer shows any trace of density from

308    the 30S subunit (Figures S15A, and D). This class mainly contains particles

309    from 900 ms (Figure 3M). The map agrees quite well with the map of HflX-

310    50S-GNP-PNP[2] (Figures S15A-C).

311    A comparison of the atomic models built for the three intermediate states

312    reveals that HflX changes its position on the ribosome and undergoes major

313    conformational changes, specifically in its CTD, HLD, and NTD. The domain

314    movements of CTD and HLD match quite well with the dynamics of apo-HflX

315    predicted from 1000 ns of molecular dynamics simulations (Methods section

316    in SI and Figure S16). Interestingly, the loop-helix motif (G74-V100) of NTD

317    makes stable contact with H71 of the 50S subunit in i70S$_{HflX}$-II (Figures 4D-

318    F).

319

320    **Dynamics of HflX and possible GTP-bound state**

321    In trying to understand the actions of HflX, we examined the hydrolyzation

322    state of GTP in the different states of HflX. At 25 ms, with the exception of

323    their NTDs, the densities of HflX and associated nucleotides in states HflX-I

13

324  and HflX-II are not resolved as well as they are for the other two states,

325  indicating mobility and preventing determination of the hydrolyzation state

326  (Figure S10). In an attempt to fit the atomic model of GTP to the corresponding

327  densities in HflX-III and HflX-IV, we observed that the density in the region

328  of the nucleotide site on HflX-III is a better fit for GDP·Pi than for either GTP

329  or GDP (Figure 5A). A similar matching effort resulted in a decent match of

330  GTP to the density of HflX bound to the 50S subunit, even though the GDP

331  state is expected to be found at this stage (Figure 5B).

332        Since at the 140 ms time point the inorganic phosphate (Pi) is still

333  associated with GDP and virtually none of the 30S subunits has been cleaved

334  off, we conclude that the energy for the breaking of bridges B3 and B7a and

335  the final dissociation of the 30S subunit is set free by the release of Pi. It is

336  unclear without further investigation if GTP hydrolysis plays a role in the

337  initial stages of splitting, from intermediate I to II, since it is known that HflX

338  can perform the splitting in the absence of GTP, albeit at a slower rate[2]. The

339  likely explanation for the observation of GTP on the 50S subunit-bound HflX

340  molecule at 900 ms is that by that time both Pi and GDP have left and that a

341  new GTP molecule has taken their place.

342

343  **Time-dependent rupturing of intersubunit bridges**

344  As the direct observation of the state of bridges from the cryo-EM map is not

345  conclusive due to resolution limitations, we proceeded with a geometric

346  calculation to estimate the sequence in which intersubunit bridges are ruptured.

347  With the axes and angles of the 30S subunit rotation known, as well as the

348  locations of all bridges relative to the axes, we were able to determine the

349　distances between constituent residues of all intersubunit bridges. From these

350　distances and known ranges of chemical bond lengths we were able to estimate

351　at which time points the intersubunit bridges are likely disrupted and broken

352　(Figure 5D). According to these calculations, bridges B1a, B1b, B2a, and B2b

353　are already disrupted at 10 ms. Bridges B5, B6, B7b, and B7bR are disrupted

354　between 10 and 25 ms. All these bridges are found to be broken within 140 ms.

355　Finally, the last two bridges, B3 and B7a, which form the hinges of Axis II,

356　give way at some time point between 140 ms and 900 ms. Bridge B4

357　(H34:uS15) presents an interesting case as it behaves like a spring: its 50S

358　subunit constituent H34 is initially compressed in the step from apo-70S to

359　i70S$_{HflX}$-I, as HflX is accommodated within the first 10 ms, but in the next two

360　steps (10 ms to 25 ms to 140 ms) it is extended (Figure 5C). This bridge finally

361　breaks along with B3 and B7a after 140 ms and, in 50S$_{HflX}$, helix H34 has

362　returned to its original position as in apo-70S.

363

## Discussion

365　Here, we present a method for preparing time-resolved cryo-EM grids to

366　capture intermediates on the ~10 to 1,000-ms timescale. Different in design

367　from those by Lu et al.[16,17], Mäeotset al.[13], and Kontziampasis et al.[14], the

368　microfluidic chip assembly comprises three replaceable modules: (1) a PDMS-

369　based internally SiO$_2$-coated micro-mixer of the splitting-and-recombination

370　(SAR) type, for efficiently mixing two samples without significant problems

371　from protein adsorption; (2) a glass capillary micro-reactor for defining the

372　reaction time, and (3) a PDMS-based micro-sprayer for depositing the reaction

373　product onto the EM-grid. The sample is subsequently vitrified by fast

374 plunging of the grid into the cryogen so that the TR cryo-grid can be well
375 prepared.

376

377 In our application to the study of HflX-mediated ribosome recycling, a
378 bacterial defense response to stress, we have demonstrated how our method is
379 able to capture, on-the-fly, high-resolution structures of intermediates that
380 represent snapshots of an unfolding complex molecular mechanism. Based on
381 our cumulative observations from the examination of three short-lived reaction
382 intermediates, we propose that the initial binding of HflX within 10 ms is
383 followed by a stepwise clamshell-like opening of the ribosome around an axis
384 that closely aligns with helix 44 of the 30S subunit, and that rupture of the last
385 two remaining intersubunit bridges, B3 and B7a, occurs after 140 ms and most
386 probably as a result of Pi release.

387

388 **Further applications of time-resolved cryo-EM in the study of functional**
389 **dynamics**
390 Our study will spur interest in the community for extending these studies to
391 recycling in the 80S ribosome by protein factors such as ABCE1 to structurally
392 reveal an evolutionarily conserved mechanism. We believe, moreover, that the
393 quantitative description of our results on a dynamic process – employing tensor
394 analysis to determine the tilt axis and rotation of subunits, and quantifying the
395 timing of intersubunit breakage – as well as the application of this microfluidic
396 device will open a new direction in the characterization of molecular events by
397 cryo-EM and will stimulate interest and draw considerable attention among a
398 wide audience of structural biologists, microbiologists, and pharmacologists.

16

399  Ultimately, it may help in the design of a new class of broad-spectrum

400  antibiotics that are able to overcome antibiotic resistance.

401

402  **Limitations of the Study**

403

404  **Limitation in time range:** Our method of TRCEM has been proven powerful

405  for capturing structural intermediates for HflX-mediated ribosome recycling

406  and other processes of translation, but there are many other interesting

407  biochemical processes awaiting visualization by this method.  Those involving

408  motions of large domains of macromolecules are excellent candidates.

409  Signaling, activation and gating mechanisms of receptors and transporters[29-31]

410  come to mind, as well, but in many cases the characteristic times of motions

411  are much shorter than 10 ms, the minimum reached by our method of mixing-

412  spraying-plunging. In this time domain, entirely different technologies have to

413  be considered[15,19,32,33]

414

415  **Limitation in the accuracy of kinetic information.** As we pointed out

416  before[10], TRCEM, in addition to furnishing the high-resolution structures of

417  reaction intermediates, has at least in principle the capacity to give kinetic

418  information, as well, since the numbers of particles in each structural class are

419  known. However, this information is currently not very accurate since it

420  depends on the vagaries of particle picking and classification strategies.

421  Investment in a search for quantitative, reproducible strategies would therefore

422  be of enormous value.

423

17

**Inefficiency of data collection.** Data collection on droplet-covered TRCEM grids remains quite time-consuming even with the proposed strategy to target certain regions close to the grid bar, since it still relies on visual/manual selection. There is clearly a need for sophisticated automatic targeting tools on grids prepared by spraying with sample droplets.

**Large required sample quantity.** Compared with conventional blotting method, the TRCEM method requires a substantially bigger volume of sample (~10 μL versus 3 μL ) for each grid, which is the minimum quantity of fluid required to reside in the whole microfluidic system for ensuring a stabilized spray. However, much of the spray is wasted in the present setup with a single EM grid as target, and an obvious next step is the development of a plunger with multiple pairs of tweezers or a specially designed tweezer-manifold to hold several grids at once.

**Unresolved questions regarding the mechanism of HflX action**. Our TRCEM analysis about the interaction between HflX and 70S ribosome leaves open the question of how HflX recognizes the stalled state of the ribosome. Here our observation of 30S subunit head rotation from apo-70S to i70SHflX-I may offer a clue. Puromysine-treated polysomes, having deacylated tRNA in the P-site, display greatly enhanced HflX splitting activity, and this state was proposed as the natural substrate for HflX[2]. In this state, the ribosome is known to undergo spontaneous intersubunit rotation[34], which goes hand in hand with 30S subunit head 'swivel' rotation[35]. This would suggest that HflX initially binds to the ribosome in its rotated conformation and forces it into the

18

449  unrotated conformation observed in i70SHflX-I, with residual 30S subunit

450  head rotation still retained. Another similarity holds if our hypothesis of HflX

451  binding to the rotated ribosome is correct since the latter is the substrate of

452  RRF/EF-G-GTP binding, as well[36,37]. But to answer these questions more

453  extensive studies with similar tools are required.

454

455

456

457

458

459

460
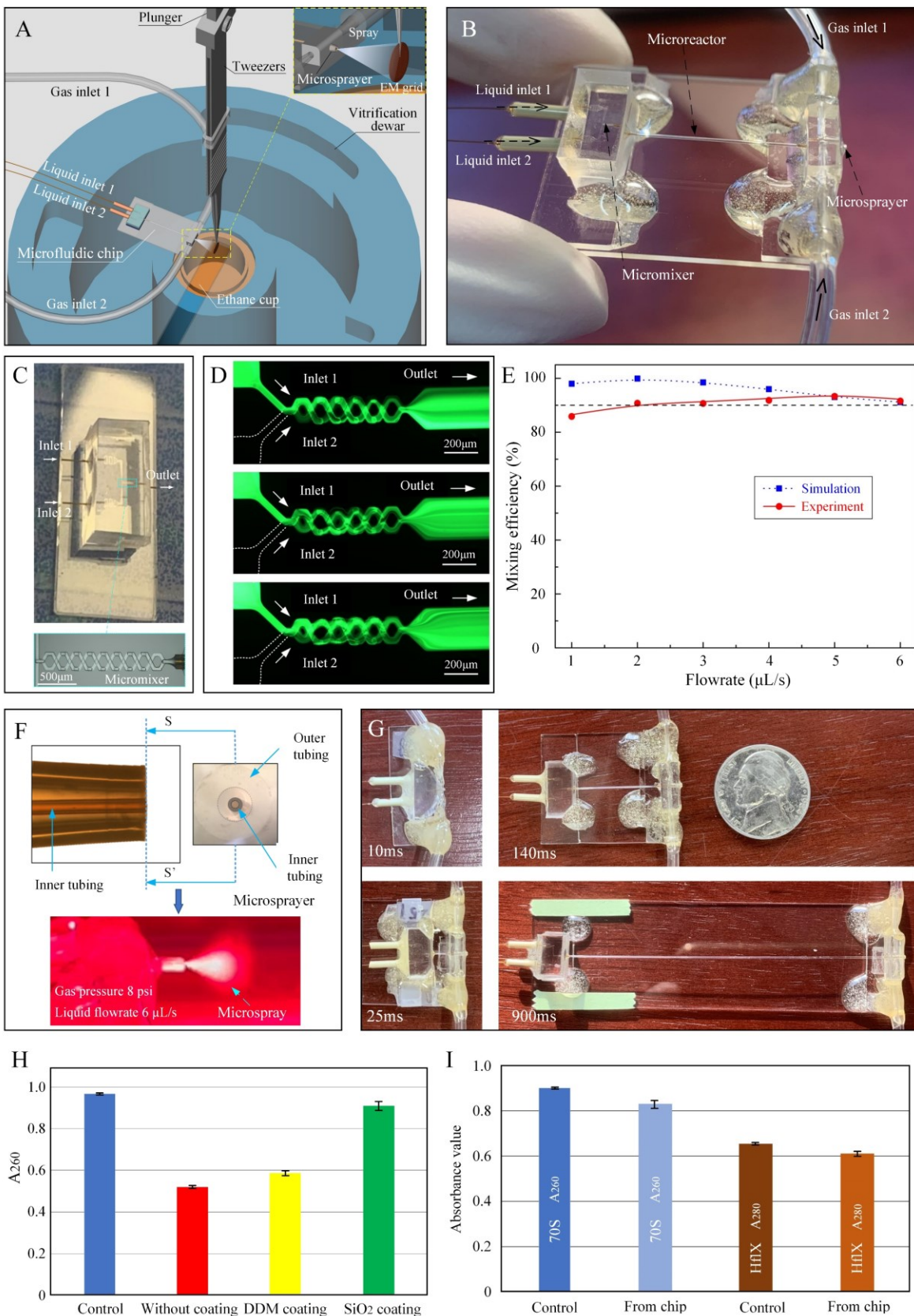
461

462

463

464

465

466

467

468

469

470

471

472

473

474

475

476

477

478

479  **FIGURES**



480

481 **Figure 1. The modular PDMS-based microfluidic chip assembly for TRCEM sample**

482 **preparation.** (A) Schematic showing the setup for TRCEM using the mixing-spraying-plunging

483 method. (B) The microfluidic chip assembly comprises three parts: micro-mixer, micro-reactor

484 and micro-sprayer. (C) The splitting-and-recombination (SAR) based micro-mixer is fabricated by

485 soft-lithography. (D) Fluorescence distribution along the micromixer with five mixing units under

486 different inlet flow rate conditions. The mixing efficiency is characterized by the evenness in the

487 distribution of fluorescent fluid. (E) Mixing efficiency for the micro-mixer at the exit under

488 different flow rate conditions. The high mixing performance of this micro-mixer was validated

489 both numerically and experimentally. (F) Micro-sprayer, with inner and outer tubing aligned and

490 centered, used for depositing the reaction product onto the grid. The micro-spray (illuminated by

491 red laser) is generated under the conditions of liquid flow rate 6 µL/s and gas pressure 8 psi, (G)

492 A set of microfluidic chips was employed to achieve required reaction time points of 10, 25, 140,

493 and 900 ms for the HflX study. (H) Compared with PDMS surface without any coating layer, and

494 with DDM coating, the $SiO_2$ coating shows effective mitigation of protein adsorption (*E. coli* 70S

495 is used as sample). (I) The $SiO_2$ coating functions well even after one month (here both *E. coli* 70S

496 and HflX are used as samples).
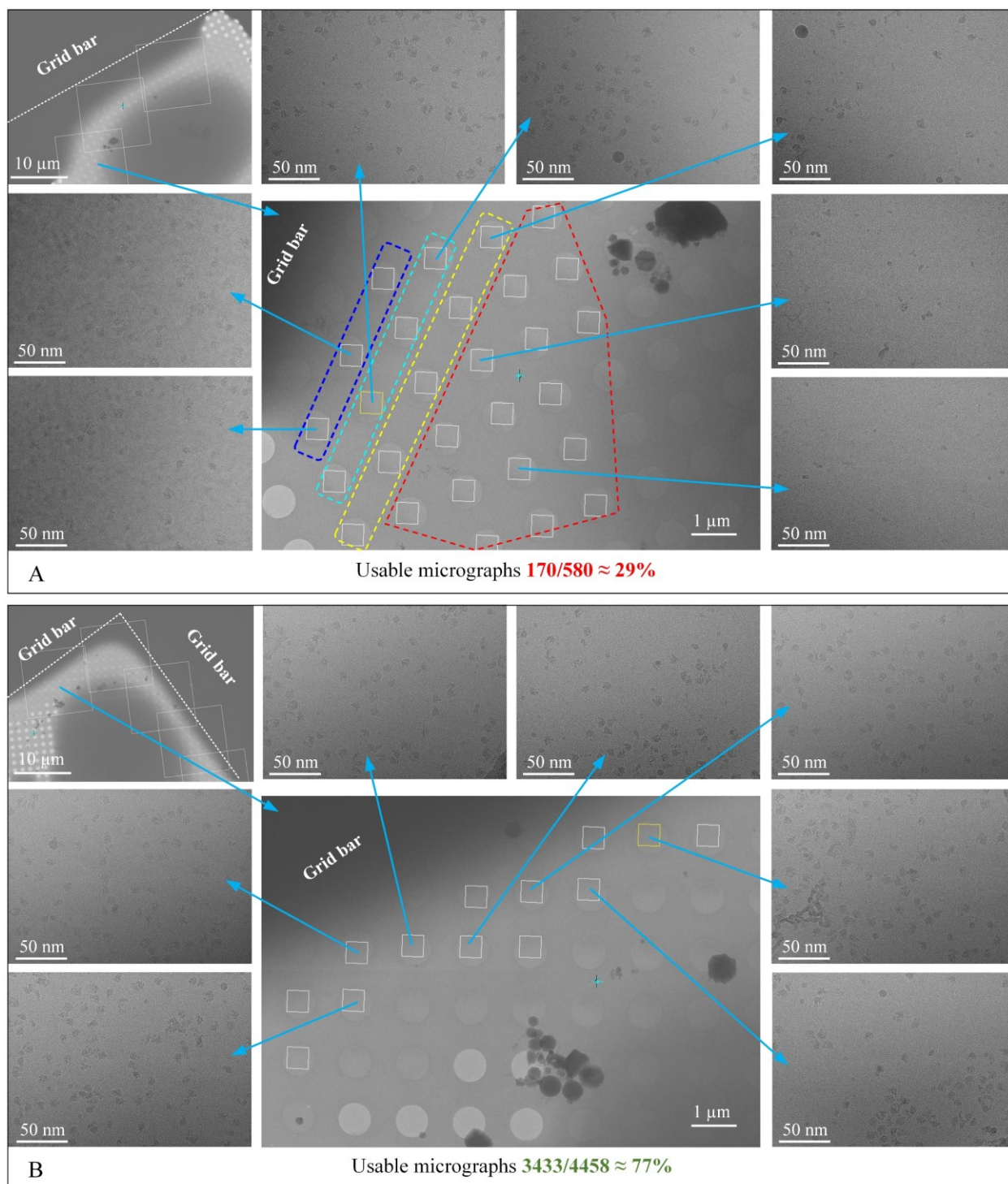
**Figure 2. Data collection strategies on droplet-based cryo-grid prepared by mixing-spraying TRCEM method.** (A) Collect as many micrographs as possible on each droplet. The number of particles gradually decreases when the target moves away from the grid bar, in the direction of

501    areas marked in blue, cyan, yellow and red. (B) Collect only along two or three lines of holes

502    which are near and parallel to the grid bar.
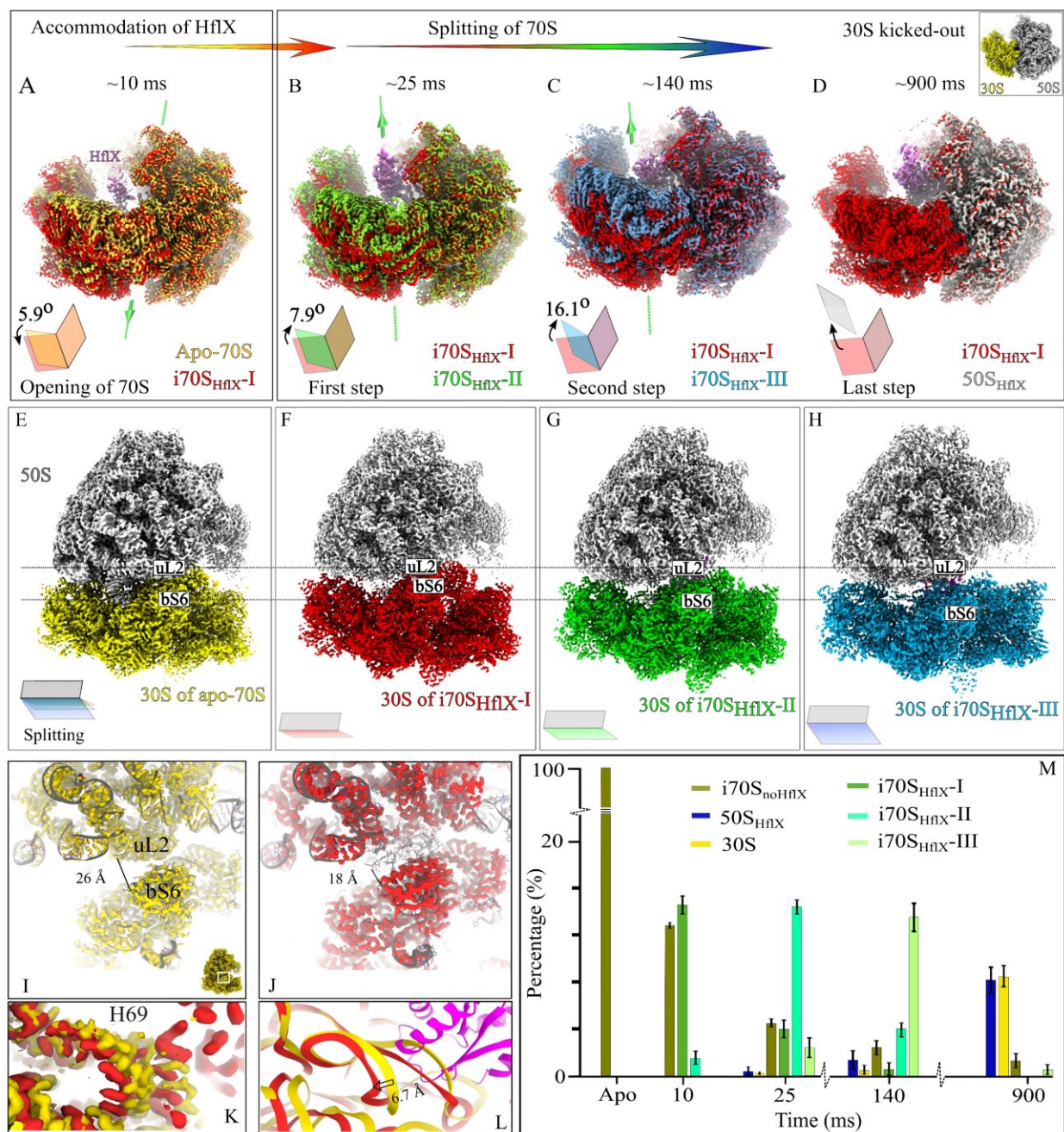
503

504

505

506

507

508

**Figure 3. Molecular details of subunit interface during the progressive opening of the 70S**

(**A**) Superimposition of reconstructions to show the opening of the 30S subunit from apo-70S (yellow) to i70S$_{HflX}$-I (red) to accommodate HflX. The green line represents the initial axis of 30S rotation, Axis I. (**B**) and (**C**), reconstructions of second and third intermediates overlapped with first intermediate, showing the stepwise splitting of the 70S by HflX by rotation of the 30S subunit around Axis II (green line). The corresponding rotation angles and direction of 30S rotation are shown in cartoon book representations. (**D**), reconstruction of the 50S-HflX complex after the

517     departure of the 30S subunit, overlapped with the first 70S intermediate.  In (**A**) through (**D**), all

518     reconstructions are aligned on the 50S subunit. (**E**) to (**H**) are the high-resolution densities of

519     control 70S at 900 ms and three intermediates obtained within 140 ms, and showing the stepwise

520     rotation of 30S during recycling with respect to 50S (gray). (**I**) and (**J**) are the zoomed views of

521     Coulomb densities in yellow for apo-70S and red for i70S$_{HflX}$-I, respectively, and corresponding

522     atomic models (gray) showing the rearrangement of the protein uL2 of the 50S and bS6 of 30S to

523     accommodate HflX. (**K**) and (**L**), Coulomb densities, and corresponding ribbon models of H69

524     from apo-70S (yellow), and i70S$_{HflX}$-I (red), respectively, showing the very first movement of

525     helix H69. HflX is shown in magenta. (**M**) Kinetics of the splitting reaction in terms of the number

526     of particles per class as a function of time, obtained by 3D classification.
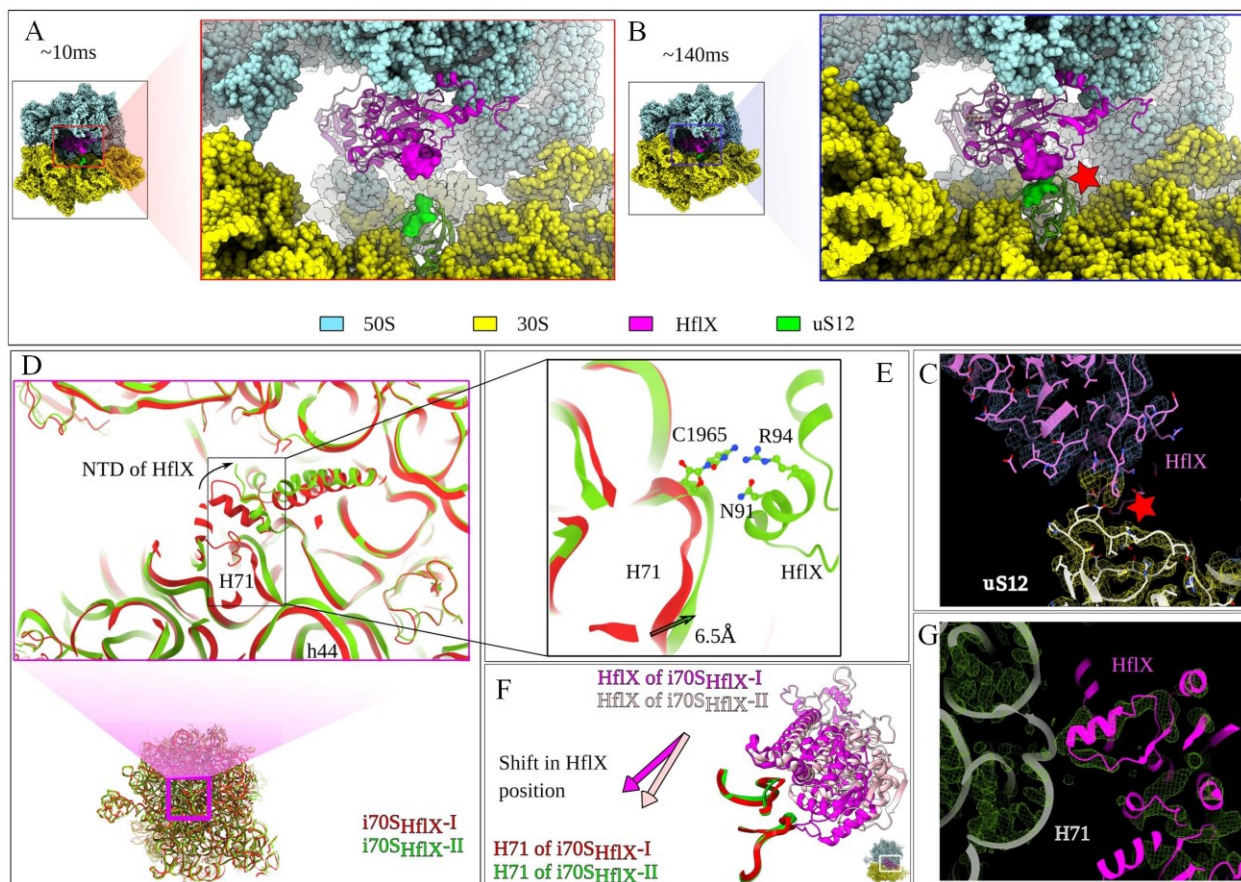
527

528

529

530

531

532

533

534

535

536

**Figure 4. The shift of S12 towards HflX and Involvement of HflX in 70S splitting**

The zoomed view of HflX and S12 of 30S interactions from i70SHflX-I and i70SHflX-III states are shown in (**A**) and (**B**), respectively. Due to the stepwise separation of the 30S during splitting, there occurs a steric clash (red star) at 140 ms due to the subsequent shift of the whole S12, which is not present at earlier states like10 ms, and this clash is the cause of the final separation of 30S from 50S by a power-stroke from HflX upon GTP hydrolysis. (**C**) The same clash at 140 ms from i70SHflX-III is shown in Coulomb density with a fitted model. (**D**) Pulling of H71 by the NTD of HflX causes the disruption of intersubunit bridge B3 between H71 and h44, and the zoomed view in (**E**) shows the interacting residues of both H71 and HflX. During pulling of H71 HflX has to shift its position and is shown in (**F**). (**G**) The same interaction is shown in Coulomb density with a fitted model.

26

552



553
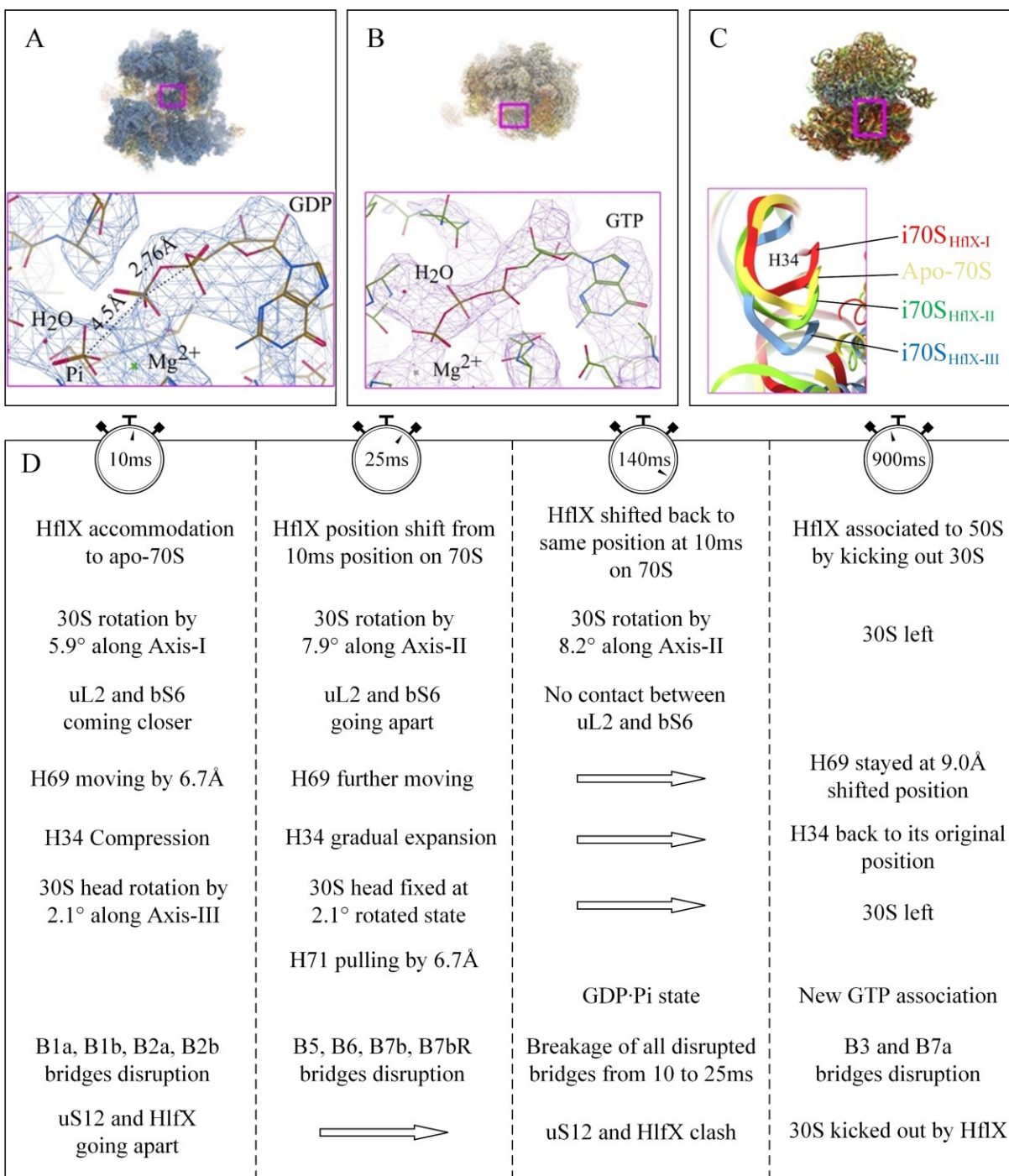
**Figure 5. Analysis of nucleotide states, and spring-like nature of H34 and molecular events**

(**A**) Refined density map of i70S$_{HflX}$-III (in mesh) with an atomic model fitted in with the zoomed

view of i70S$_{HflX}$-III with the fitted model of GTP • Pi. The distance of 4.5 Å between GDP and

557     Pi is compared with the distance of 2.8 Å between two P atoms of GDP. This distance between

558     GDP and Pi is too large to form a P-O bond as in GTP. (**B**) Refined density map of $50S_{HflX}$ (in

559     mesh) with atomic model fitted in along with the zoomed view of $50S_{HflX}$ with the fitted model of

560     GTP. (**C**) The superimposition of atomic models of apo-70S and three intermediates with the

561     zoomed view of H34 showing its spring-like behavior. Corresponding colors are indicated. (**D**)

562     The molecular events involved during the 70S splitting by HflX are tabulated.

563

564

565

29
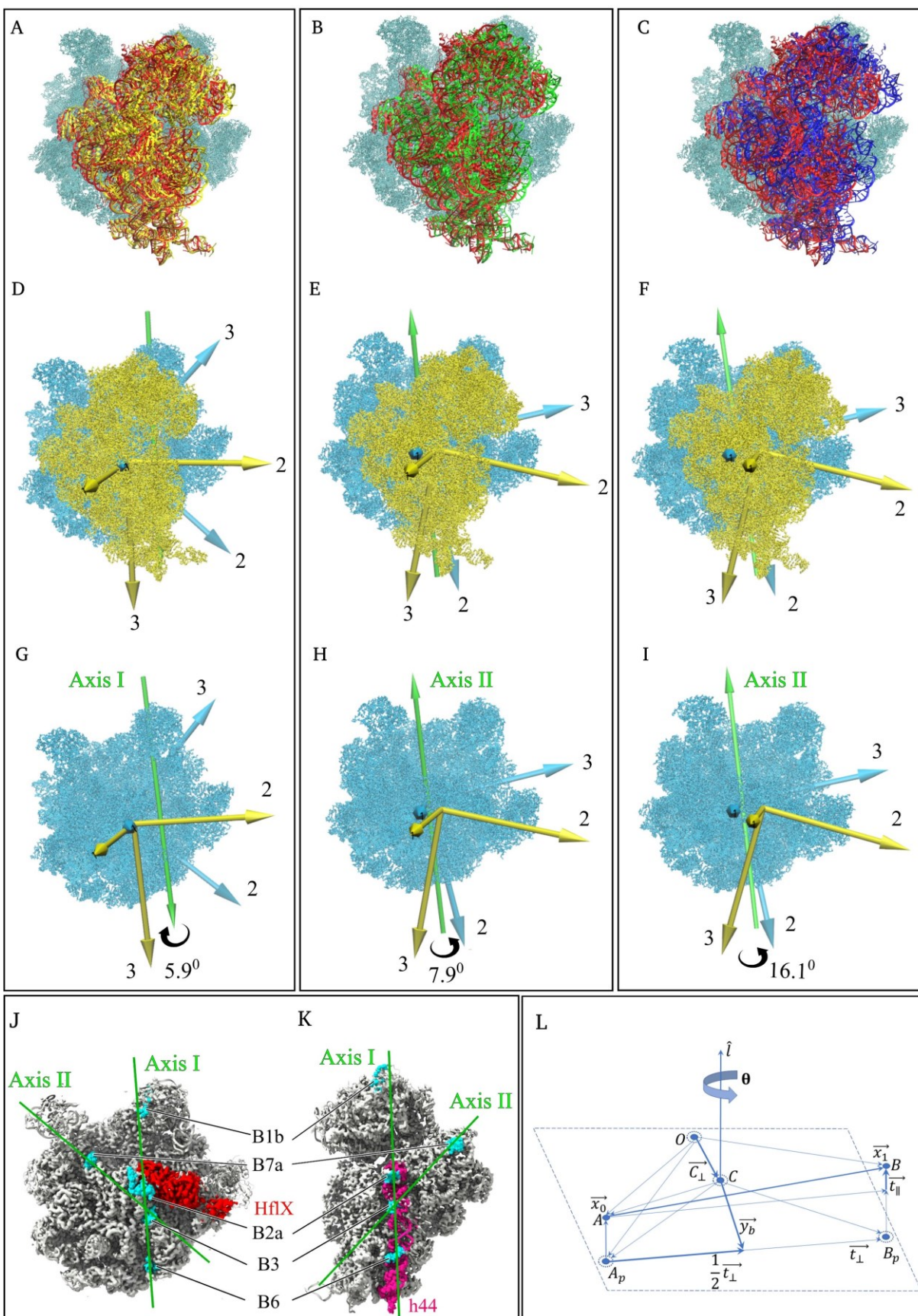
566   **Figure 6**. **Axes of rotation of 30S subunit during splitting/recycling of the 70S ribosome: (A),**
567   **(B)**, and **(C)**, rotation of 30S subunit from Apo-70S (yellow) to i70S$_{HflX}$-I (red), i70S$_{HflX}$-I (red) to
568   i70S$_{HflX}$-II (green), and i70S$_{HflX}$-I (red) to i70S$_{HflX}$-III (blue), respectively. **(D)**, **(E)**, and **(F)**
569   characterization of the 30S subunit rotation while the 50S subunits (cyan) are fixed in space. The
570   models show the rotated state of the 30S subunit in each case. For clarity, 30S subunits are
571   represented with only their principal axes of inertia. Rotation axes (Axis I, Axis II) are shown as
572   green arrows indicating the direction (right-hand thumb rule) of the rotation (black curled arrows).
573   **(D)** Rotation by 5.9° of 30S subunit around Axis I from Apo-70S (yellow) to i70S$_{HflX}$-I (red). **(E)**
574   and **(F)**, Rotations by 7.9° and 16.1°, respectively, of 30S subunit around Axis II. **(G)**, **(H)**, and
575   **(I)**, same representation as **(D)**, **(E)**, and **(F)** omitting the 30S subunit to show the axes clearly. **(J)**
576   and **(K)**, Intersubunit bridges through which Axes I and II pass on the 50S and 30S subunit,
577   respectively. **(L)** Formulation of rigid body motion along with location of the rotation axis. Initial
578   and transformed positions are respectively denoted by A (position vector $\vec{x}_0$) and B (position
579   vector $\vec{x}_1$). The shift from A to B is given by translation vector $\vec{t}$. Points with dotted circles are
580   on the plane perpendicular to the rotation axis $\hat{l}$. Points $\overrightarrow{A_p}$ and $\overrightarrow{B_p}$ are projections of points A
581   and B, respectively. $\vec{t}_{\parallel}$ and $\vec{t}_{\perp}$ are respectively the parallel and perpendicular components of the
582   translation vector $\vec{t}$. Axis $\hat{l}$ and angle $\theta$ describes the rotation of the rigid body from point A to B.
583   The rotation axis $\hat{l}$ passes through the point given by the position vector $\vec{C}_{\perp}$. The solution for the
584   position vector $\vec{C}_{\perp}$ is obtained by using the remaining vectors, as indicated in the derivation in
585   Methods Section in SI "Determining the position vector of the unique point through which the
586   rotation axis passes".

587

588

589

590   Supplemental video 1. Spraying and plunging during the TR experiment.

591

592   Supplemental video 2. The clamshell-like splitting of the ribosome from Intermediate I over
593   Intermediates II and III, ending with the 50S subunit (shown) and the 30S subunit (not shown), the
594   end products of the recycling process.

595

30

596

## Acknowledgements

604

## Author contributions

S.B., X.F., and J.F. conceived the research; S.B., X.F., and J.F. designed the experiments; S.B. prepared the biological samples; X.F. designed the TR chips; X.F., and P.D., developed the chip; X.F., S.B., performed the TR cryo-EM experiments; S.B., X.F., and Z.Z. collected the Cryo-EM data; S.B. processed the data; S.M. calculated the subunit and domain motions and the axes of rotation; Z.P.B. helped S.B. with atomic model building and validation, S.B., X.F., and J.F. wrote the manuscript with the help of S.M. for Methods.

613

## Declaration of interest

Columbia University has filed patent applications related to this work for which X.F. and J.F. are inventors.

617

## Data and code availability

The refined maps are deposited on EMDB and corresponding atomic models on PDB and will be publicly available as of the date of publication.

621 EMD-29681 (control apo-70S at 900ms), 29688 (i70S$_{HflX}$-I), 29687 (i70S$_{HflX}$-

622 II), 29689 (i70S$_{HflX}$-III), 29833 (consensus i70S$_{HflX}$-I, 30S focused), 29834

623 (i70S$_{HflX}$-I, 50S focused and 30S subtracted), 29724 (consensus i70S$_{HflX}$-II, 30S

624 focused), 29844 (i70S$_{HflX}$-II, 50S focused and 30S subtracted), 29723 (consensus

625 i70S$_{HflX}$-III, 30S focused), 29842 (i70S$_{HflX}$-III, 50S focused and 30S subtracted).

626

627 PDB- 8G2U (control apo-70S at 900ms), 8G34 (i70S$_{HflX}$-I), 8G31 (i70S$_{HflX}$-II),

628 8G38 (i70S$_{HflX}$-III).

629

630 **References:**

631 1.     Gao, N., Zavialov, A.V., Li, W., Sengupta, J., Valle, M., Gursky, R.P.,
632        Ehrenberg, M., and Frank, J. (2005). Mechanism for the disassembly of the
633        posttermination complex inferred from cryo-EM studies. Mol Cell *18*, 663-
634        674. https://doi.org/10.1016/j.molcel.2005.05.005.

635 2.     Zhang, Y., Mandava, C.S., Cao, W., Li, X., Zhang, D., Li, N., Zhang, Y.,
636        Zhang, X., Qin, Y., Mi, K., et al. (2015). HflX is a ribosome-splitting factor
637        rescuing stalled ribosomes under stress conditions. Nat Struct Mol Biol *22*,
638        906-913. https://doi.org/10.1038/nsmb.3103.

639 3.     Koripella, R.K., Deep, A., Agrawal, E.K., Keshavan, P., Banavali, N.K., and
640        Agrawal, R.K. (2021). Distinct mechanisms of the human mitoribosome
641        recycling and antibiotic resistance. Nat Commun *12*, 3607.
642        https://doi.org/10.1038/s41467-021-23726-4.

643 4.     Brito Querido, J., Sokabe, M., Kraatz, S., Gordiyenko, Y., Skehel, J.M.,
644        Fraser, C.S., and Ramakrishnan, V. (2020). Structure of a human 48S
645        translational initiation complex. Science *369*, 1220-1227.
646        https://doi.org/10.1126/science.aba4904.

647 5.     Frank, J. (2017). Time-resolved cryo-electron microscopy: Recent progress.
648        J Struct Biol *200*, 303-306. https://doi.org/10.1016/j.jsb.2017.06.005.

649    6.    Chen, B., and Frank, J. (2016). Two promising future developments of cryo-
650          EM: capturing short-lived states and mapping a continuum of states of a
651          macromolecule. Microscopy (Oxf) *65*, 69-79.
652          https://doi.org/10.1093/jmicro/dfv344.

653    7.    Dandey, V.P., Budell, W.C., Wei, H., Bobe, D., Maruthi, K., Kopylov, M.,
654          Eng, E.T., Kahn, P.A., Hinshaw, J.E., Kundu, N., et al. (2020). Time-
655          resolved cryo-EM using Spotiton. Nat Methods *17*, 897-900.
656          https://doi.org/10.1038/s41592-020-0925-6.

657    8.    Chen, B., Kaledhonkar, S., Sun, M., Shen, B., Lu, Z., Barnard, D., Lu, T.M.,
658          Gonzalez, R.L., Jr., and Frank, J. (2015). Structural dynamics of ribosome
659          subunit association studied by mixing-spraying time-resolved cryogenic
660          electron microscopy. Structure *23*, 1097-1105.
661          https://doi.org/10.1016/j.str.2015.04.007.

662    9.    Fu, Z., Kaledhonkar, S., Borg, A., Sun, M., Chen, B., Grassucci, R.A.,
663          Ehrenberg, M., and Frank, J. (2016). Key Intermediates in Ribosome
664          Recycling Visualized by Time-Resolved Cryoelectron Microscopy.
665          Structure *24*, 2092-2101. https://doi.org/10.1016/j.str.2016.09.014.

666    10.   Kaledhonkar, S., Fu, Z., Caban, K., Li, W., Chen, B., Sun, M., Gonzalez,
667          R.L., Jr., and Frank, J. (2019). Late steps in bacterial translation initiation
668          visualized using time-resolved cryo-EM. Nature *570*, 400-404.
669          https://doi.org/10.1038/s41586-019-1249-5.

670    11.   Kaledhonkar, S., Fu, Z., White, H., and Frank, J. (2018). Time-Resolved
671          Cryo-electron Microscopy Using a Microfluidic Chip. Methods Mol Biol
672          *1764*, 59-71. https://doi.org/10.1007/978-1-4939-7759-8_4.

673    12.   Klebl, D.P., White, H.D., Sobott, F., and Muench, S.P. (2021). On-grid and
674          in-flow mixing for time-resolved cryo-EM. Acta Crystallogr D Struct Biol
675          *77*, 1233-1240. https://doi.org/10.1107/S2059798321008810.

676    13.   Maeots, M.E., Lee, B., Nans, A., Jeong, S.G., Esfahani, M.M.N., Ding, S.,
677          Smith, D.J., Lee, C.S., Lee, S.S., Peter, M., and Enchev, R.I. (2020).
678          Modular microfluidics enables kinetic insight from time-resolved cryo-EM.
679          Nat Commun *11*, 3465. https://doi.org/10.1038/s41467-020-17230-4.

680    14.   Kontziampasis, D., Klebl, D.P., Iadanza, M.G., Scarff, C.A., Kopf, F.,
681          Sobott, F., Monteiro, D.C.F., Trebbin, M., Muench, S.P., and White, H.D.

682    (2019). A cryo-EM grid preparation device for time-resolved structural
683    studies. IUCrJ *6*, 1024-1031. https://doi.org/10.1107/S2052252519011345.

684  15.  Berriman, J., and Unwin, N. (1994). Analysis of transient structures by cryo-
685    microscopy combined with rapid mixing of spray droplets. Ultramicroscopy
686    *56*, 241-252. https://doi.org/10.1016/0304-3991(94)90012-4.

687  16.  Lu, Z., Shaikh, T.R., Barnard, D., Meng, X., Mohamed, H., Yassin, A.,
688    Mannella, C.A., Agrawal, R.K., Lu, T.M., and Wagenknecht, T. (2009).
689    Monolithic microfluidic mixing-spraying devices for time-resolved cryo-
690    electron microscopy. J Struct Biol *168*, 388-395.
691    https://doi.org/10.1016/j.jsb.2009.08.004.

692  17.  Lu, Z., Barnard, D., Shaikh, T.R., Meng, X., Mannella, C.A., Yassin, A.,
693    Agrawal, R., Wagenknecht, T., and Lu, T.M. (2014). Gas-Assisted Annular
694    Microsprayer for Sample Preparation for Time-Resolved Cryo-Electron
695    Microscopy. J Micromech Microeng *24*, 115001.
696    https://doi.org/10.1088/0960-1317/24/11/115001.

697  18.  Knoska, J., Adriano, L., Awel, S., Beyerlein, K.R., Yefanov, O., Oberthuer,
698    D., Pena Murillo, G.E., Roth, N., Sarrou, I., Villanueva-Perez, P., et al.
699    (2020). Ultracompact 3D microfluidics for time-resolved structural biology.
700    Nat Commun *11*, 657. https://doi.org/10.1038/s41467-020-14434-6.

701  19.  Torino, S., Dhurandhar, M., Stroobants, A., Claessens, R., and Efremov,
702    R.G. (2022). Time-resolved cryo-EM using a combination of droplet
703    microfluidics with on-demand jetting. bioRxiv, 2022.2010. 2021.513149.
704    https://doi.org/10.1101/2022.10.21.513149.

705  20.  Noble, A.J., Dandey, V.P., Wei, H., Brasch, J., Chase, J., Acharya, P., Tan,
706    Y.Z., Zhang, Z., Kim, L.Y., and Scapin, G. (2018). Routine single particle
707    CryoEM sample and grid characterization by tomography. Elife *7*, e34257.

708  21.  Verstraeten, N., Fauvart, M., Versees, W., and Michiels, J. (2011). The
709    universally conserved prokaryotic GTPases. Microbiol Mol Biol Rev *75*,
710    507-542, second and third pages of table of contents.
711    https://doi.org/10.1128/MMBR.00009-11.

712  22.  Coatham, M.L., Brandon, H.E., Fischer, J.J., Schummer, T., and Wieden,
713    H.J. (2016). The conserved GTPase HflX is a ribosome splitting factor that
714    binds to the E-site of the bacterial ribosome. Nucleic Acids Res *44*, 1952-
715    1961. https://doi.org/10.1093/nar/gkv1524.

716   23.   Rudra, P., Hurst-Hess, K.R., Cotten, K.L., Partida-Miranda, A., and Ghosh,
717         P. (2020). Mycobacterial HflX is a ribosome splitting factor that mediates
718         antibiotic resistance. Proceedings of the National Academy of Sciences *117*,
719         629-634.

720   24.   Dey, S., Biswas, C., and Sengupta, J. (2018). The universally conserved
721         GTPase HflX is an RNA helicase that restores heat-damaged Escherichia
722         coli ribosomes. J Cell Biol *217*, 2519-2529.
723         https://doi.org/10.1083/jcb.201711131.

724   25.   Feng, X., Fu, Z., Kaledhonkar, S., Jia, Y., Shah, B., Jin, A., Liu, Z., Sun, M.,
725         Chen, B., Grassucci, R.A., et al. (2017). A Fast and Effective Microfluidic
726         Spraying-Plunging Method for High-Resolution Single-Particle Cryo-EM.
727         Structure *25*, 663-670.e663. https://doi.org/10.1016/j.str.2017.02.005.

728   26.   Hirokawa, G., Iwakura, N., Kaji, A., and Kaji, H. (2008). The role of GTP in
729         transient splitting of 70S ribosomes by RRF (ribosome recycling factor) and
730         EF-G (elongation factor G). Nucleic Acids Res *36*, 6676-6687.
731         https://doi.org/10.1093/nar/gkn647.

732   27.   Frank, J., and Agrawal, R.K. (2000). A ratchet-like inter-subunit
733         reorganization of the ribosome during translocation. Nature *406*, 318-322.
734         https://doi.org/10.1038/35018597.

735   28.   Maji, S., Shahoei, R., Schulten, K., and Frank, J. (2017). Quantitative
736         Characterization of Domain Motions in Molecular Machines. J Phys Chem
737         B *121*, 3747-3756. https://doi.org/10.1021/acs.jpcb.6b10732.

738   29.   Simsir, M., Broutin, I., Mus‑Veteau, I., and Cazals, F. (2021). Studying
739         dynamics without explicit dynamics: A structure‑based study of the export
740         mechanism by AcrB. Proteins: structure, function, and bioinformatics *89*,
741         259-275. https://doi.org/10.1002/prot.26012.

742   30.   Gangwar, S.P., Yen, L.Y., Yelshanskaya, M.V., and Sobolevsky, A.I.
743         (2023). Positive and negative allosteric modulation of GluK2 kainate
744         receptors by BPAM344 and antiepileptic perampanel. Cell Reports *42*.
745         https://doi.org/10.1016/j.celrep.2023.112124.

746   31.   Qiu, W., Fu, Z., Xu, G.G., Grassucci, R.A., Zhang, Y., Frank, J.,
747         Hendrickson, W.A., and Guo, Y. (2018). Structure and activity of lipid
748         bilayer within a membrane-protein transporter. Proceedings of the National

749      Academy of Sciences *115*, 12985-12990.
750      https://doi.org/10.1073/pnas.1812526115.

751 32.   Harder, O.F., Barrass, S.V., Drabbels, M., and Lorenz, U.J. (2023). Fast
752      viral dynamics revealed by Microsecond Time-Resolved Cryo-EM. bioRxiv,
753      2023.2004. 2019.536710.

754 33.   Voss, J.M., Harder, O.F., Olshin, P.K., Drabbels, M., and Lorenz, U.J.
755      (2021). Rapid melting and revitrification as an approach to microsecond
756      time-resolved cryo-electron microscopy. Chemical Physics Letters *778*,
757      138812.

758 34.   Valle, M., Zavialov, A., Sengupta, J., Rawat, U., Ehrenberg, M., and Frank,
759      J. (2003). Locking and unlocking of ribosomal motions. Cell *114*, 123-134.
760      https://doi.org/10.1016/s0092-8674(03)00476-8.

761 35.   Ratje, A.H., Loerke, J., Mikolajka, A., Brünner, M., Hildebrand, P.W.,
762      Starosta, A.L., Dönhöfer, A., Connell, S.R., Fucini, P., and Mielke, T.
763      (2010). Head swivel on the ribosome facilitates translocation by means of
764      intra-subunit tRNA hybrid sites. Nature *468*, 713-716.
765      https://doi.org/10.1038/nature09547.

766 36.   Agrawal, R.K., Sharma, M.R., Kiel, M.C., Hirokawa, G., Booth, T.M.,
767      Spahn, C.M., Grassucci, R.A., Kaji, A., and Frank, J. (2004). Visualization
768      of ribosome-recycling factor on the Escherichia coli 70S ribosome:
769      functional implications. Proceedings of the National Academy of Sciences
770      *101*, 8900-8905. https://doi.org/10.1073/pnas.0401904101.

771 37.   Dunkle, J.A., Wang, L., Feldman, M.B., Pulk, A., Chen, V.B., Kapral, G.J.,
772      Noeske, J., Richardson, J.S., Blanchard, S.C., and Cate, J.H.D. (2011).
773      Structures of the bacterial ribosome in classical and hybrid states of tRNA
774      binding. Science *332*, 981-984. https://doi.org/10.1126/science.1202692.
775